Available online at www.sciencedirect.com
ScienceDirect
International Journal of Thermal Sciences 47 (2008) 1332–1346
International Journal of Thermal Sciences
www.elsevier.com/locate/ijts

The effect of flow field and turbulence on heat transfer characteristics of confined circular and elliptic impinging jets

M.F. Koseoglu [a,*], S. Baskaya [b]

[a] *Department of Mechanical Engineering, Pamukkale University, 20070 Kınıklı, Denizli, Turkey*
[b] *Department of Mechanical Engineering, Gazi University, 06570 Maltepe, Ankara, Turkey*

Received 23 July 2007; received in revised form 22 October 2007; accepted 26 October 2007

Available online 20 February 2008

Abstract

The flow field of confined circular and elliptic jets was studied experimentally with a Laser Doppler Anemometry (LDA) system. In addition, heat transfer characteristics were numerically investigated. Experiments were conducted with a circular jet and an elliptic jet of aspect ratio four, jet to target spacings of 2 and 6 jet diameters, and Reynolds number 10 000. The toroidal recirculation pattern was observed in the outflow region for both geometries at dimensionless jet to plate distance 2. Higher spreading rates in the minor axis direction of the elliptic jet have also been mapped. Along the target plate, different boundary layer profiles were obtained for circular and elliptic jets at $H/d = 2$, but profiles became similar when dimensionless jet to plate distance was increased to 6. Positions of maximum radial and axial velocities and turbulence intensities have been determined for both geometries. For the confined circular and elliptic jet geometries, analysis of flow field measurements and numerical heat transfer results showed that inner peaks in local heat transfer closely relate to turbulence intensities in the jet and radial flow acceleration along the wall. Differences between the circular and elliptic jet, in terms of flow field and heat transfer characteristics, reduced with increase in the jet to plate distance.

Keywords: Confined impinging jet; Circular; Elliptic; Electronic cooling; CFD; LDA

1. Introduction

Impinging jets are used in many applications where high heat and mass transfer rates are required. Applications include thermal management of electronics equipment, gas turbine blade cooling, glass tempering and annealing, paper and cereal drying.

Extensive prior research has been conducted to understand flow and heat transfer characteristics of impinging jets. Viskanta and Jambunathan et al. [1,2] summarized these research. Gardon and Akfirat [3,4] have investigated the dependence of heat transfer on parameters such as Reynolds number, jet to target plate distance and turbulence for the range of *Re* numbers 450–22 000 and dimensionless jet to plate distances 1/3–80.

Heat transfer characteristics of impinging jets depend also on the jet inlet geometry. The elliptic jet is intermediate between axisymmetric jet and plane jet. Depending on aspect ratio it either becomes an axisymmetric jet or a plane jet. But elliptic jets are more complex than plane or circular jets because of its two geometric dimensions (Hussain and Husain [5]).

Most of the earlier elliptic jet studies were for free jets. In an experimental study with elliptic free jets Ho and Gutmark [6] determined that the entrainment ratio of an elliptic jet was several times greater than that of a circular jet. They also observed significantly different turbulence properties in the major and minor axis planes. In another study with free elliptic jets Hussain and Husain [5] investigated water and air jets. With flow visualization experiments they observed that the spreading rate is larger in the minor axis plane than in the major axis and determined axis switchover at some downstream position. They also stated that "elliptic jets are quite different from circular jets owing mainly to the fact that the azimuthal curvature variation of a vortical structure causes its non-uniform self induction and

* Corresponding author. Tel.: +90 312 2317400 ext. 2470; fax: +90 312 2308434.
E-mail address: mehmetfevzi@gazi.edu.tr (M.F. Koseoglu).

1290-0729/$ – see front matter
doi:10.1016/j.ijthermalsci.2007.10.015

Nomenclature

a, b	radius of major and minor axis of elliptic jet
A_s	heat source surface area ..... m^2
C_1, C_2, C_μ	empirical constants in turbulence model
d	jet diameter
EJ1	circular jet
EJ4	elliptic jet with aspect ratio four
f_1, f_2, f_μ	damping functions in the low Reynolds number model
H/d	dimensionless jet to target plate distance
k	thermal conductivity ..... W/mK
k	turbulent kinetic energy
L	turbulence length scale
N	number of velocity samples
Nu	local Nusselt number
p	static pressure
Pe	Peclet number, $Pe = Re\,Pr$
q_c	convection heat flux ..... W/m^2
Re	Reynolds number, $Re = (W_{jet}d)/\nu_{air}$
Re_t, Re_y	turbulence Reynolds numbers
t_i	transit time of the ith seeding particle
T	temperature ..... °C
T_{jet}	jet inlet temperature
T_u	turbulence intensity
u_i, u_j	arbitrary velocity components
u_τ	friction velocity
u, v, w	velocity components in x, y, z directions
u_{rms}	radial rms velocity
w_{rms}	axial rms velocity
U_i, U_j	time averaged arbitrary velocity components
W_{jet}	jet inlet velocity ..... m/s
x/d	dimensionless distance from impinging point along the major axis
y/d	dimensionless distance from impinging point along minor axis
z/d	dimensionless distance from target plate in the axial direction
z	distance from the target plate
z^+	dimensionless distance $z^+ = (u_\tau z\rho/\mu)$

Greek symbols

ρ	density ..... kg/m^3
μ, μ_t	laminar and eddy dynamic viscosities .... kg/ms
ν, ν_t	laminar and eddy kinematic viscosities .... m^2/s
η	transit time weighting factor
ε	dissipation rate of turbulent kinetic energy
$\sigma_k, \sigma_\varepsilon$	turbulent Prandtl numbers

Subscripts

air	air
jet	jet inlet

Superscript

$'$	fluctuation

hence complex three-dimensional deformation. Such deformation, combined with properly selected excitation can substantially alter entrainment and other turbulence phenomena."

Lee et al. [7] investigated elliptic impinging jets of aspect ratio 2.14. They obtained higher Nusselt number values for the elliptic jet than the circular jet in the impingement region. They also determined second and third maxima in Nusselt number distribution for $H/D = 2$ at $Re = 10\,000$ and $20\,000$. The effect of elliptic jet aspect ratio, on stagnation region heat transfer has been investigated by Lee and Lee [8]. One of the rare studies with elliptic jet arrays with 3 different exit conditions was the subject of research by Yan et al. [9]. Local heat transfer characteristics of elliptic jet arrays with different aspect ratios $(4, 2, 1, 0.5, 0.25)$ were determined and also axis switchover phenomenon with cross flow effect was found for elliptic jet aspect ratios greater than 1. In related experimental studies by Yan et al. [10] and Yan and Mei [11], they investigated heat transfer characteristics along rib-roughened walls for circular and elliptic impinging jet arrays by using transient liquid crystal technique. They determined that the heat transfer over the rib surface may be enhanced or retarded depending on the orientation of the ribs and the highest heat transfer rate was obtained with 45 degree V-shape ribs.

The impinging jet is an interesting flow in practice as well as providing a demanding test case for turbulence modeling. Craft et al. [12] summarized the main flow characteristics as: "the motion in the vicinity of the stagnation point comprises a nearly irrotational normal straining (rather than simple shearing), while that nearer the edge of the impinging jet combines strong rotationality and streamline curvature. Finally, further from the impinging point the flow does revert to a thin shear flow by no means to a simple one, with the maximum shear stress occurring outside the wall region". Because of the above mentioned complexity in the flow and simple geometry which can be easily handled from a numerical point of view, many numerical studies have been conducted on impinging jet flow and heat transfer.

In the numerical study with confined impinging jets Hosseinalipour and Mujumdar [13] were able to predict the stagnation region Nusselt numbers with low Reynolds number k–ε models. In another study by Wang and Mujumdar [14], they tested several low Re number k–ε models for confined turbulent slot jets. They found models perform better for high jet to plate distances. Shi et al. [15] numerically studied impingement heat transfer under a turbulent slot jet using standard k–ε and RMS models. For turbulent jet impingement studies, three second moment closure type models and one eddy viscosity model were compared by Craft et al. [12]. They stated that both the eddy viscosity model and the basic Reynolds stress model achieved very poor agreement with experiments. Near wall reflection model results were in better agreement with experiments. Dianat et al. [16] also have found that the second

moment closure model generally performs better than the standard k–ε model with wall functions. Low Reynolds number q–ζ model was applied by Gibson and Harper [17] for impinging jet heat transfer, and they stated that even though model retains the deficiency of excessive turbulence energy level, it performed better than the corresponding k–ε model.

In their studies with confined jets Fitzgerald and Garimella and Garimella [18,19] stated that the flow field in confined jets were very different from that of unconfined jets. The aim of this study is to determine the flow field of confined circular and elliptic impinging jets with detailed velocity and turbulence measurements and use these measurements to explain the local heat transfer characteristics obtained numerically.

2. Experimental set-up and data reduction

Information on the experimental apparatus, devices used and procedures followed were given in detail by Koseoglu [20]. A summary of that information is presented below.

2.1. Experimental set-up

Schematic representation of the experimental set-up was shown in Fig. 1. The whole assembly including LDA measurement system, 3-D traverse mechanism, target plate assembly, jet plate, plenum, and blower were fixed on a table for rigidity purposes. The required flow rate was supplied by a centrifugal blower. In order to obtain the desired flow rate for the *Re* number of interest a frequency controller (SIEMENS, CINAMICS G110) was connected to the blower. The rest of the set-up was acoustically isolated from the blower with flexible hosing and dampers. Velocity measurements were made with a DANTEC 2-D LDA system. The system operates in backscatter mode and was used in conjunction with a 300 mW Argon Ion laser. Bragg cell and color separator was used for frequency shifting and color separation of the laser beam from the Argon Ion laser. The back-scattered light was captured by the transmitting/receiving optics in laser probe (transceiver) which was mounted on LDA traverse mechanism and a photomultiplier converts the light intensity fluctuations to electrical signals. Electrical signals were converted to velocity information in the Burst Spectrum Analyzer (BSA) signal processor. The processing results were handled by the Burst Spectrum Analyzer (BSA) flow software. The blower was connected to the plenum with a pipe of 900 mm length and 20 mm inner diameter. Air was carried to the plenum through the connecting pipe from the blower. Plenum made of 10 mm thick Plexiglas was a 800 mm long rectangular duct with an inner square cross-section of 100×100 mm. 200 mm portion of lower end section of the plenum was cut off to easily mount and demount the orifice plates containing the jet. A sharp edged orifice type circular jet (EJ1) with a diameter of 10 mm and an elliptic jet of aspect ratio four (EJ4) with equivalent diameter of 10 mm was drilled on two separate $200 \times 120 \times 3$ mm orifice plates by laser cutting technique with centers located at 50 mm from the sides and from the end of the plenum. The length of the major and minor axis of elliptic jet was 20 and 5 mm respectively. In the experiments a uniform flow was achieved at the jet exit. To satisfy this condition, flow was almost brought to rest in the large plenum prior to the jet exit. In addition to that, orifice plate thickness was limited to 3 mm to prevent flow development which could damage uniform flow conditions. The target plate assembly consists of target plate, resistance heater, thermocouples, insulation and traverse mechanism. Target plate material was copper with dimensions of $100 \times 100 \times 5$ mm. The whole target plate assembly was fixed on a 3-D traverse system which was used to set the desired jet to target plate distance.

2.2. Processing of the experimental data

In the experimental part of the study, detailed velocity and turbulence measurements were made with the DANTEC 2-D LDA system for a circular jet (EJ1) and an elliptic jet (EJ4) of the same equivalent diameter (10 mm) with an aspect ratio of four. Measurements were obtained for jet to plate distances of 2 and 6 at Reynolds number 10 000. DANTEC 2-D LDA system operates in backscatter mode with the receiving optics mounted in the same probe as the transmitting optics and is used in conjunction with a 300 mW Argon Ion laser. The focal length of the transmitting lens was 400 mm. Frequency shifting was used to improve the data rate and to reduce the fringe bias. Data was converted from analog to digital by DANTEC-BSA-F60 signal processor and then fed to a personal computer for analysis with BSA flow software. Olive oil was used as

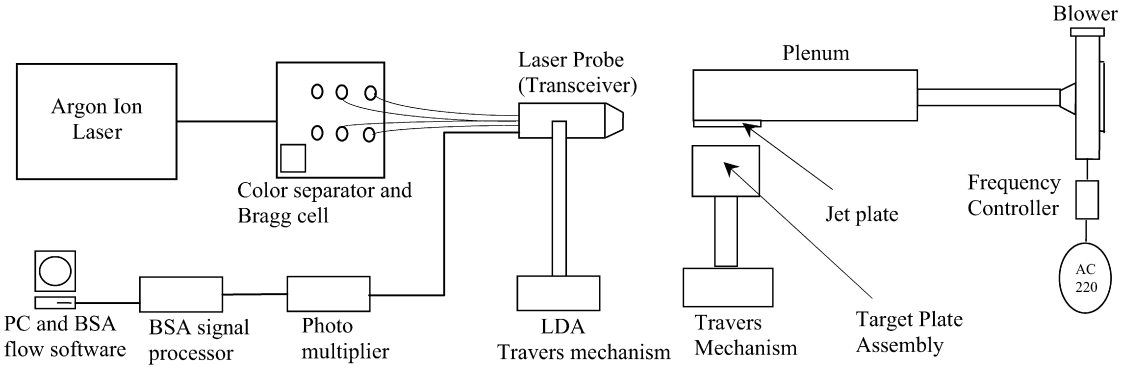

Fig. 1. Schematic diagram of the experimental set-up.

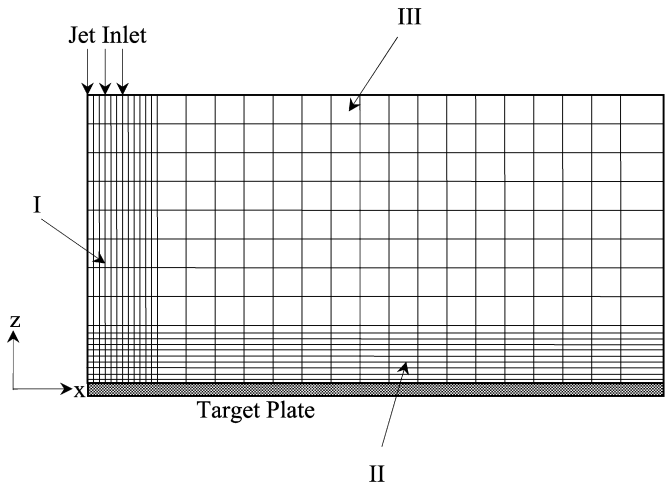

Fig. 2. LDA measurement grid structure.

seeding particle and generated by a seeding generator equipped with Laskin nozzles. Around five thousand data points were taken at each position to determine local, mean velocity and turbulence level. Laser probe was mounted on a computer controlled traverse mechanism and was traversed to within 0.1 mm. Due to the obstruction of laser beams by the orifice and target plate axial velocities very near these plates could not be obtained. Measurements were conducted at an half domain because of symmetry. As shown in Fig. 2 in region I, the axial velocity component was measured in a region starting at the jet centerline and extending over 1 jet diameter for circular jet and short axis direction of elliptic jet. The axial velocity component measurements in the long axis direction of elliptic jet were extended to 2 jet diameters. In this region radial velocities were also measured to obtain velocity vectors. In region II which was chosen close to the target plate, only radial velocity components were measured, in a region starting from the centerline of the jet and extending to the end of the impinging plate at increasing uniform distances from the impinging plate. First measurement position was at 0.02d from the target plate. More measurement locations were set in this region to map the boundary layer development. Measurements in region II have been obtained for circular jet and for the major axis direction of elliptic jet. In order to obtain the velocity vector distribution in the whole flow field, both radial and axial velocity components in region III have been measured. The whole measurement grid distribution is shown in Fig 2. Before and during the measurements to minimize the velocity bias, set up of the LDA system was made according to the directions in the LDA systems user manual [21]. Frequency shifting was used to improve the data rate, and transit time weighting factor was applied to reduce the velocity bias. Also to obtain enough seeding particles at an acceptable size, the seeding generator was equipped with a compressor. As a result, error in the velocity measurements were estimated to be below 2% according to the literature [18], theoretical basis of the method [22] and LDA system's user manual [21].

Mean, rms velocities and Reynolds shear stresses were obtained from the following equations:

- Mean velocity:

$$\bar{u} = \sum_{i=0}^{N-1} \eta_i u_i \tag{1}$$

where u_i is the instantaneous velocity and η_i is the transit time weighting factor defined as:

$$\eta_i = \frac{t_i}{\sum_{j=0}^{N-1} t_j} \tag{2}$$

where N is the number of velocity samples, and t_i is the transit time of the ith seeding particle passing the LDA measuring volume.

- Rms velocity:

$$u_{\mathrm{rms}} = \sqrt{\overline{\sum_{i=0}^{N-1} \eta_i (u_i - \bar{u})^2}} \tag{3}$$

- Reynolds shear stress:

$$\overline{u'v'} = \sum_{i=0}^{N-1} \eta_i (u_i - \bar{u})(v_i - \bar{v}) \tag{4}$$

where u_i and v_i are instantaneous velocity components.

3. Mathematical formulation and numerical model

In this section numerical description of the problem under investigation is given. Mathematical formulation, boundary conditions and solution methodology have been shortly described.

3.1. Problem description

A schematic drawing of the confined impinging jet configuration under investigation and the actual computational domain used for the numerical simulations is shown in Fig. 3. Because of symmetry, solutions were obtained for only one quarter of the domain shown with dashed lines. The equivalent diameter of the elliptic jets (d) was defined as the diameter of a circular jet with a momentum flux equal to that of an elliptic jet, $d = 2(a * b)^{0.5}$. According to Hussain and Husain [5], it is the most appropriate length scale for elliptic jets of moderate aspect ratio.

3.2. Governing equations

The continuity, Reynolds averaged momentum and time averaged energy equations governing 3-D steady, flow of air with constant properties used for turbulent solutions can be written in the Cartesian coordinate system as follows:

- Conservation of mass:

$$\frac{\partial U_i}{\partial x_i} = 0 \tag{5}$$

- Conservation of momentum:

$$\rho U_i \frac{\partial U_j}{\partial x_i} = -\frac{\partial P}{\partial x_j} + \frac{\partial}{\partial x_i}\left[\mu\left(\frac{\partial U_i}{\partial x_j} + \frac{\partial U_j}{\partial x_i}\right) - \rho\overline{u_i' u_j'}\right] \tag{6}$$

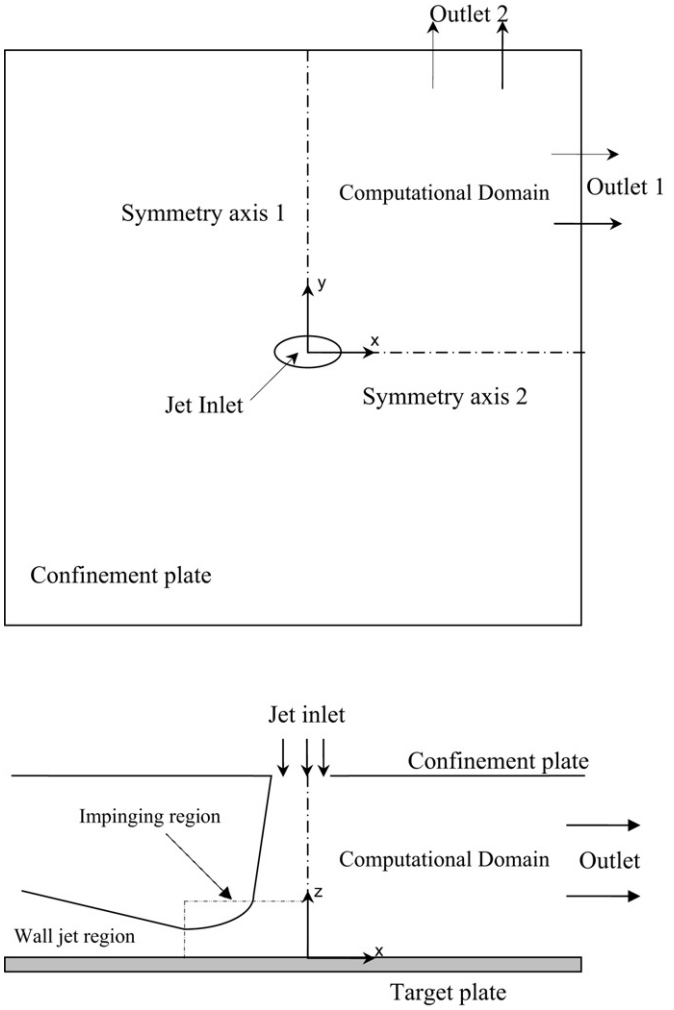

Fig. 3. Geometry of the impinging jet arrangement and computational domain employed in the simulations.

- Conservation of energy:

$$\rho c_p U_i \frac{\partial T}{\partial x_i} = \frac{\partial}{\partial x_i}\left[k\frac{\partial T}{\partial x_i} - \rho c_p \overline{u_i' T'}\right] \tag{7}$$

In the code, k–ε model developed by Launder and Spalding [23] is employed. The large scale turbulent motion is affected by fluid viscosity in low Re number flows. Effects of viscosity are important if turbulence Reynolds number is lower than 100 and damping is required to account for the viscous stresses in the viscous sublayer and low Re number regions. For this purpose, Lam–Bramhorst (LB) model allocating the low Re numbers was employed. The LB low Re number model has been widely used for impinging jet modeling [24,25]. The form of the LB model implemented in PHOENICS is that described by Patel et al. [26]. The following transport equations for k and ε are used:

$$\rho U_i \frac{\partial k}{\partial x_i} = \frac{\partial}{\partial x_i}\left[\left(\mu + \frac{\mu_t}{\sigma_k}\right)\frac{\partial k}{\partial x_i}\right] + \mu_t\left(\frac{\partial U_i}{\partial x_j} + \frac{\partial U_j}{\partial x_i}\right)\frac{\partial U_i}{\partial x_j} - \rho\varepsilon \tag{8}$$

$$\rho U_i \frac{\partial \varepsilon}{\partial x_i} = \frac{\partial}{\partial x_i}\left[\left(\mu + \frac{\mu_t}{\sigma_\varepsilon}\right)\frac{\partial \varepsilon}{\partial x_i}\right] + f_1 C_1 \mu_t \frac{\varepsilon}{k}\left(\frac{\partial U_i}{\partial x_j} + \frac{\partial U_j}{\partial x_i}\right)\frac{\partial U_i}{\partial x_j} - f_2 C_2 \rho \frac{\varepsilon^2}{k} \tag{9}$$

The eddy viscosity was calculated from:

$$\mu_t = f_\mu C_\mu \rho \frac{k^2}{\varepsilon} \tag{10}$$

The following empirical constants are used in the model:

$$\sigma_k = 1.00, \quad \sigma_\varepsilon = 1.314, \quad C_1 = 1.44, \quad C_2 = 1.92$$
$$C_\mu = 0.09 \tag{11}$$

The LB low-Reynolds-number k–ε model differs from the standard high-Reynolds-number model in that the empirical coefficients C_μ, C_1 and C_2 are multiplied by the following functions, respectively:

$$f_\mu = \left[1 - \exp(-0.0165 Re_z)\right]^2 \left(1 + \frac{20.5}{Re_t}\right) \tag{12}$$

$$f_1 = \left(1 + \frac{0.05}{f_\mu}\right)^3 \tag{13}$$

$$f_2 = 1 - \exp\left(-Re_t^2\right) \tag{14}$$

where

$$Re_z = \frac{\rho k^{1/2} z}{\mu} \tag{15}$$

$$Re_t = \frac{\rho k^2}{\mu\varepsilon} \tag{16}$$

3.3. Solution algorithm

Governing equations were discretized by a numerical scheme employing a control volume approach and finite volume equations were obtained by this approach. These equations were solved by the widely used CFD package PHOENICS, employing the SIMPLEST algorithm [27] for the pressure correction process along with the solution procedure for the hydrodynamic equations. The package uses a staggered grid arrangement. For the discretization of convective–diffusive transport, the hybrid scheme is the default scheme within the code. This scheme combines the stability of upwind-scheme with the approximation accuracy of the central-difference scheme. In the hybrid-scheme diffusion is cut off when the cell Peclet number ($Pe = Re * Pr$, i.e. the ratio of heat convection to heat conduction) equals 2. In other words, the convective transport is assumed to dominate diffusive transport, and the hybrid-scheme reduces to the upwind formulation, with diffusion terms being neglected. The central-difference scheme leads to a second-order truncation error in the approximations, whereas the upwind-scheme gives only first-order accuracy.

3.4. Boundary conditions

Fig. 3 shows the actual computational domain and the boundaries. No slip condition was accommodated along the

solid walls and flow velocities were set to zero. Turbulent kinetic energy (k) and gradient of dissipation rate with respect to z were also set to zero at the walls. Constant heat flux condition was applied at the target plate, and the confinement plate in the solution domain was considered to be adiabatic. The other applied boundary conditions were as given below.

- Inlet:

$$W_{\text{jet}} = \text{specified}, \qquad T_{\text{jet}} = \text{specified}$$
$$k_{\text{jet}} = (TuW_{\text{jet}})^2, \qquad \varepsilon = (C_\mu C_d)^{3/4} k^{3/2} L \tag{17}$$

- Symmetry axis 1 and outlet 1: x derivatives of the velocity components, temperature, k and ε are set to zero:

$$\frac{\partial u}{\partial x} = 0, \qquad \frac{\partial v}{\partial x} = 0, \qquad \frac{\partial w}{\partial x} = 0$$
$$\frac{\partial T}{\partial x} = 0, \qquad \frac{\partial k}{\partial x} = 0, \qquad \frac{\partial \varepsilon}{\partial x} = 0 \tag{18}$$

- Symmetry axis 2 and outlet 2: y derivatives of the velocity components, temperature, k and ε are set to zero:

$$\frac{\partial u}{\partial y} = 0, \qquad \frac{\partial v}{\partial y} = 0, \qquad \frac{\partial w}{\partial y} = 0$$
$$\frac{\partial T}{\partial y} = 0, \qquad \frac{\partial k}{\partial y} = 0, \qquad \frac{\partial \varepsilon}{\partial y} = 0 \tag{19}$$

3.5. Convergence and grid independency

The PHOENICS code iteratively solves linear algebraic equations resulting from the finite volume integration of the partial differential equations. Due to the iterative process of the code, convergence was used as the monitor of achievement of the final solution. The criterion of convergence of the numerical solution is based on the absolute normalized residuals of the equations that were summed for all cells in the computational domain. Convergence was considered as being achieved when these residuals become less than 10^{-7}, which was the case for most of the dependent variables. Iterative convergence was also checked by terminating the solution only then the progressive single cell values of pressure, velocity and temperature showed little change per iteration as the calculation progressed. Furthermore, checks for the achievement of a final solution were made based on the conservation of mass, momentum and energy. Trial solutions were obtained with a wide range of cell number combinations for grid independency checks. Trial solutions started with a uniform coarse grid arrangement. After that grids were refined in the jet, stagnation region and near wall regions. As a grid independency check stagnation point and average Nusselt numbers were used. Final simulations were performed with cell numbers ranging from $40 \times 40 \times 32$ to $40 \times 40 \times 64$ in the x–y–z coordinate directions depending on the jet to plate distance. Grids were refined in the jet region and close to the target surface. For turbulent solutions, to resolve the near wall region, much finer grids were set near the wall and dimensionless distance z^+ ($u_\tau z\rho/\mu$) was kept less than unity for all solutions.

4. Results and discussion

In this section, velocity and turbulence measurements are presented to describe the flow field in confined circular and elliptic jets. Local heat transfer distributions obtained from the numerical study are also presented. In figures "EJ1" and "EJ4" represents circular and elliptic jet, respectively.

Fig. 4 shows velocity vector distribution in the close vicinity of the jet center line for circular and elliptic jets. Measurements were obtained at $Re = 10\,000$ for dimensionless jet to plate distances 2 and 6. It is clearly seen that the jet spreading rate along the minor axis plane of the elliptic jet is much greater than that of the major axis, and also that of the circular jet for both jet to plate distances. As a result of the higher spreading rate in the minor axis direction, at some downstream position of the jet exit, the minor axis becomes larger than the major axis. As can be seen from the figures, for both jet to plate distances, axis-switch-over occurs around 1.2 equivalent jet diameter from the jet exit.

The presence of toroidal recirculation zone in the outflow region is a unique feature of submerged and confined jets [18]. Fig. 5 (a, b) shows the recirculation pattern which is a characteristic of the effect of the confining top plate on the flow field. At $H/d = 2$, recirculation for both circular and elliptic jets were observed. Center of the toroid was almost at the same location for both geometries. Fig. 5 (c, d) shows the flow field at $H/d = 6$. At this jet to plate spacing, no recirculation zone was observed. It could either be because of shifting of the center of the toroid to outer regions or decreasing confinement plate effect on the flow field with increasing jet to plate distance.

Velocity and turbulence measurements near the target plate are not only important for determining the flow field characteristics of elliptic and impinging jets, but also for heat transfer characteristics. Therefore besides the outflow region, in the close vicinity of the target plate surface, radial velocity components along the target plate at increasing perpendicular distances were also measured. Measurements were obtained starting from 0.02d from the target plate. Results are presented in Fig. 6 for circular and major axis direction of elliptic jet in terms of normalized radial velocities. Flow acceleration from the impinging point onwards was clearly observed for all cases. At $H/d = 2$, maximum radial velocities were obtained at $x/d = 1$ and $x/d = 0.5$ for circular and elliptic jets, respectively. For the elliptic jet maximum velocity was obtained at the closest position to target plate, which might be an indication of a thinner boundary layer for the elliptic jet. There might be an even higher velocity located nearer to the target plate. When the dimensionless jet to plate distance was increased to 6, radial velocity profiles became more similar for circular and elliptic jets. Maximum velocities were also obtained at the same radial location ($x/d = 1$).

In the impinging jets, different flow and heat transfer characteristics were observed in the stagnation region and wall jet region. To analyze these regions, radial velocity measurements near the target plate were extended to cover the whole target plate. Fig. 7 shows normalized radial velocities at locations greater than 1d along the target plate at increasing perpendic-

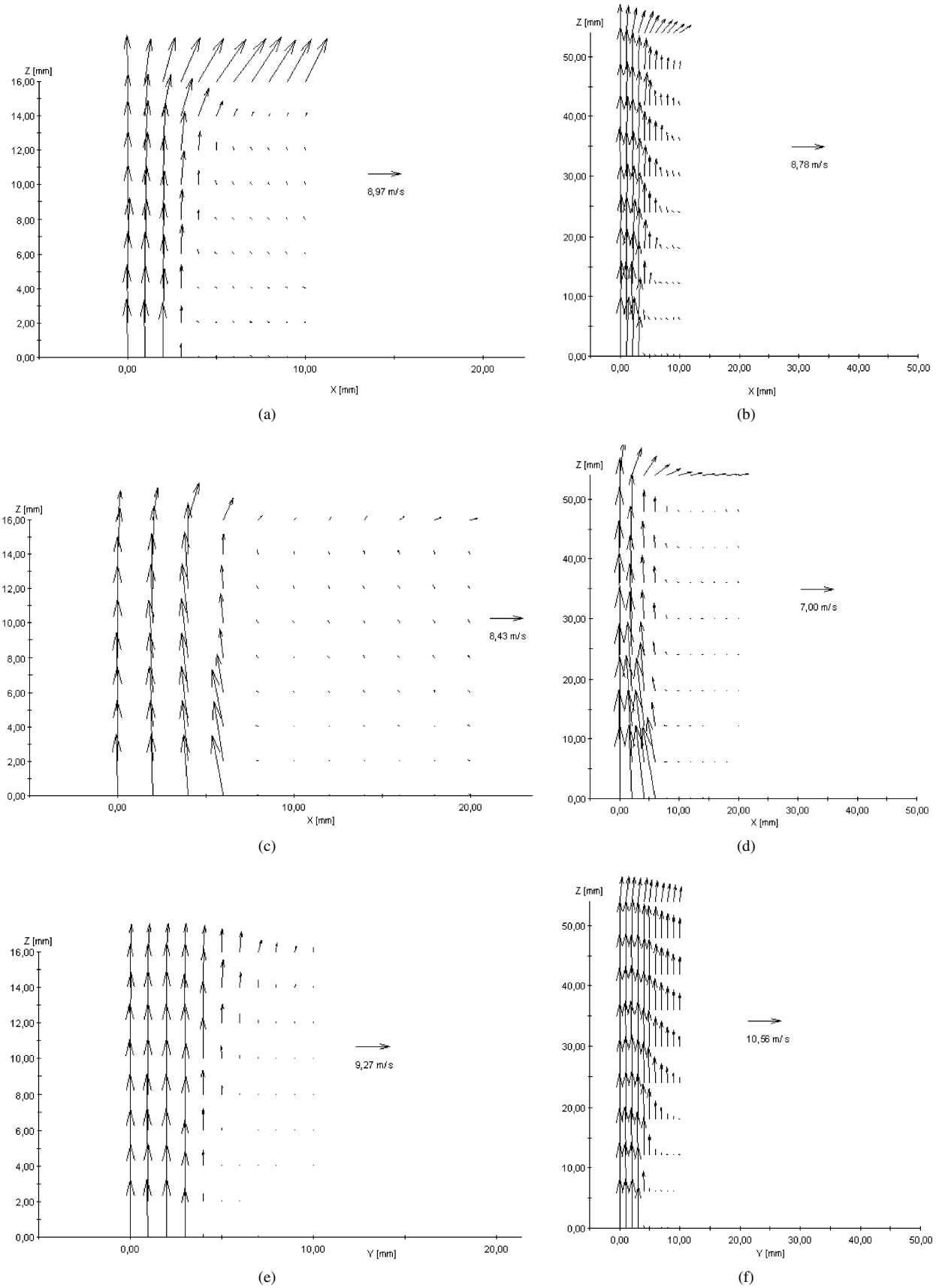

Fig. 4. LDA velocity vector distribution in the close vicinity of the jet centerline for (a) EJ1, $H/d = 2$, (b) EJ1, $H/d = 6$, (c) major axis EJ4, $H/d = 2$, (d) major axis EJ4, $H/d = 6$, (e) minor axis EJ4, $H/d = 2$, (f) minor axis EJ4, $H/d = 6$.

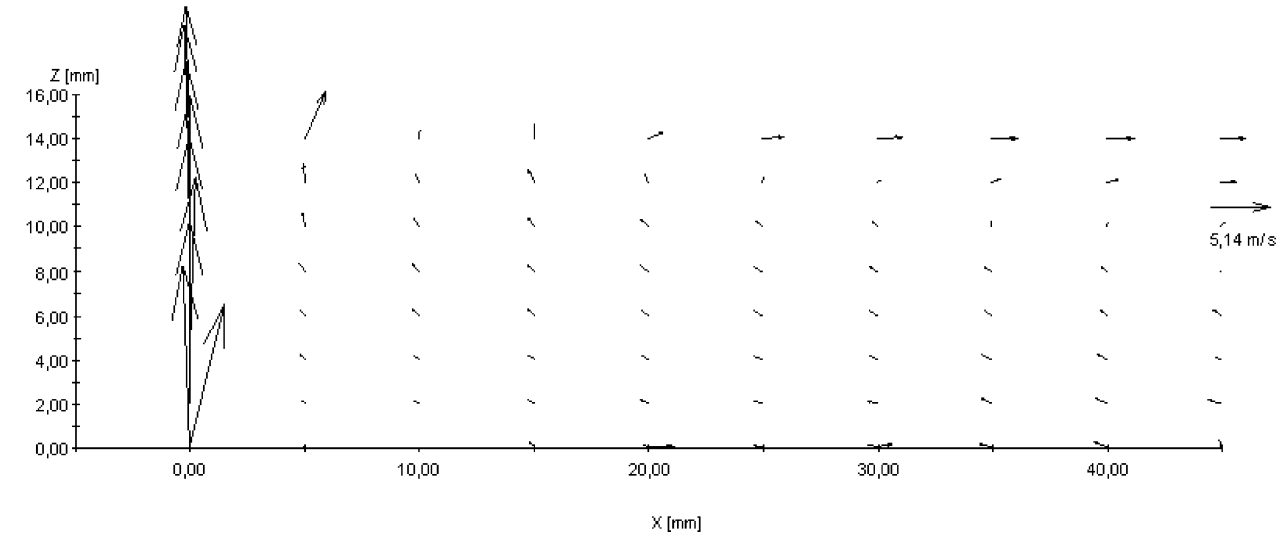

(a)

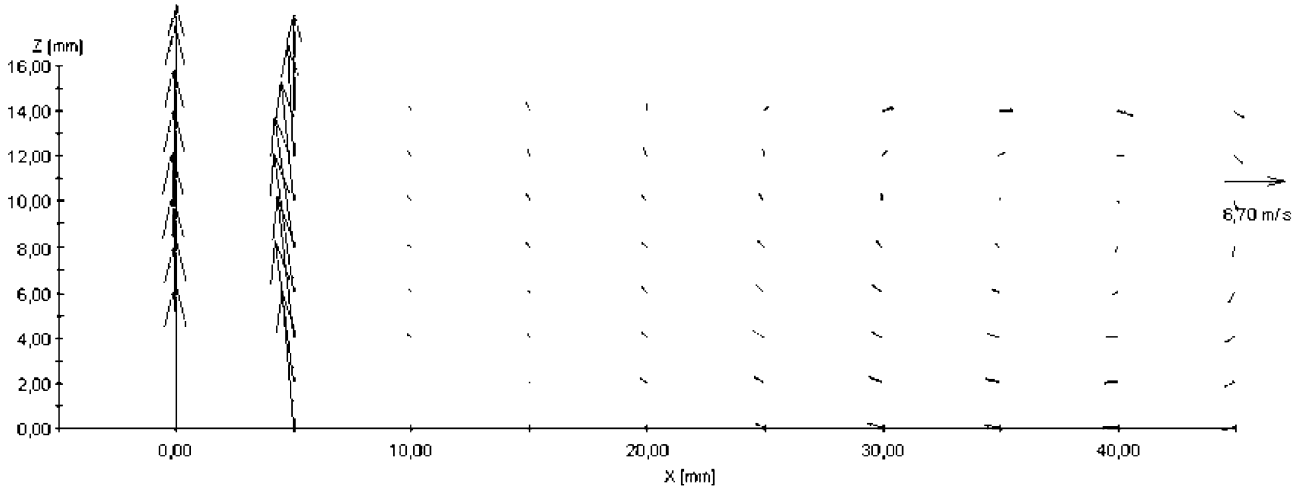

(b)

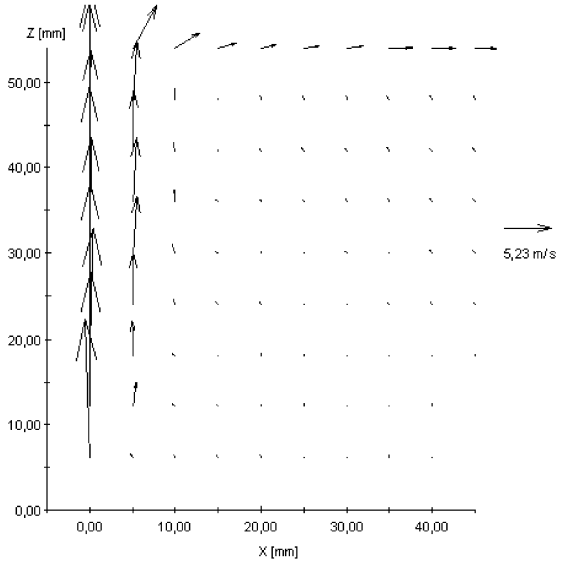

(c)

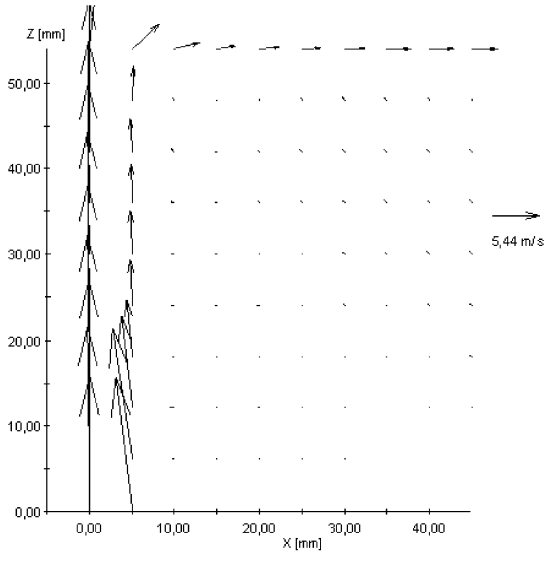

(d)

Fig. 5. LDA velocity vector distribution in the flow field for (a) EJ1, $H/d = 2$, (b) major axis EJ4, $H/d = 2$, (c) EJ1, $H/d = 6$ (d) major axis EJ4, $H/d = 6$.

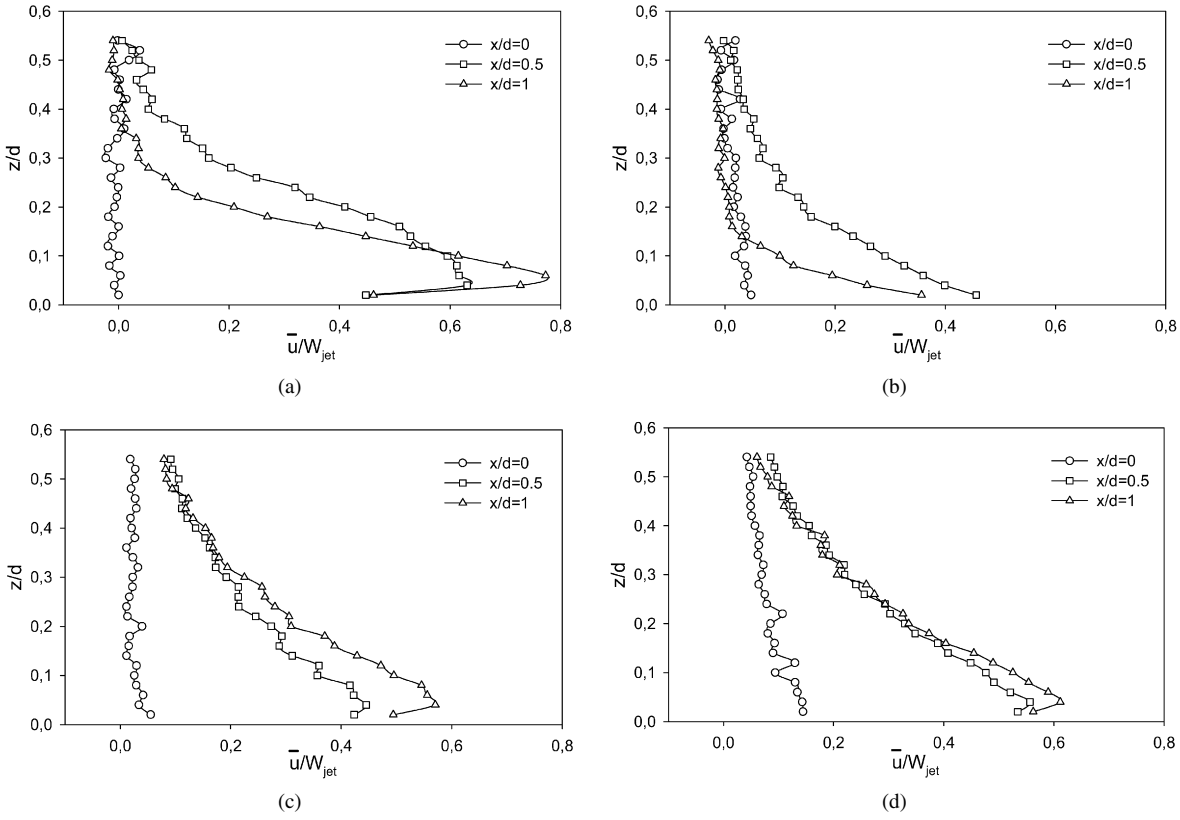

Fig. 6. LDA radial velocity distribution at $x/d = 0$–1 for (a) EJ1, $H/d = 2$, (b) major axis EJ4, $H/d = 2$, (c) EJ1, $H/d = 6$ (d) major axis EJ4, $H/d = 6$. (The target plate is located at $z/d = 0$.)

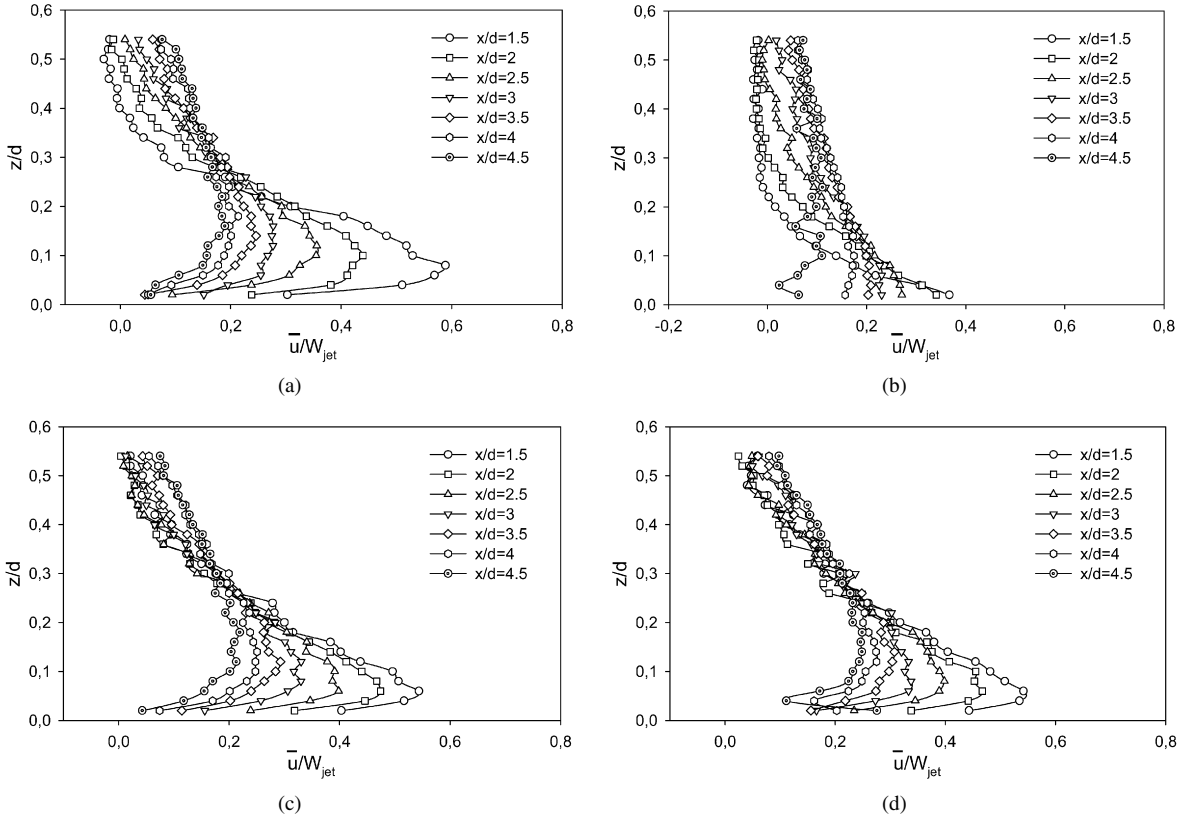

Fig. 7. LDA radial velocity distribution at $x/d = 1.5$–4.5 for (a) EJ1, $H/d = 2$, (b) major axis EJ4, $H/d = 2$, (c) EJ1, $H/d = 6$, (d) major axis EJ4, $H/d = 6$. (The target plate is located at $z/d = 0$.)

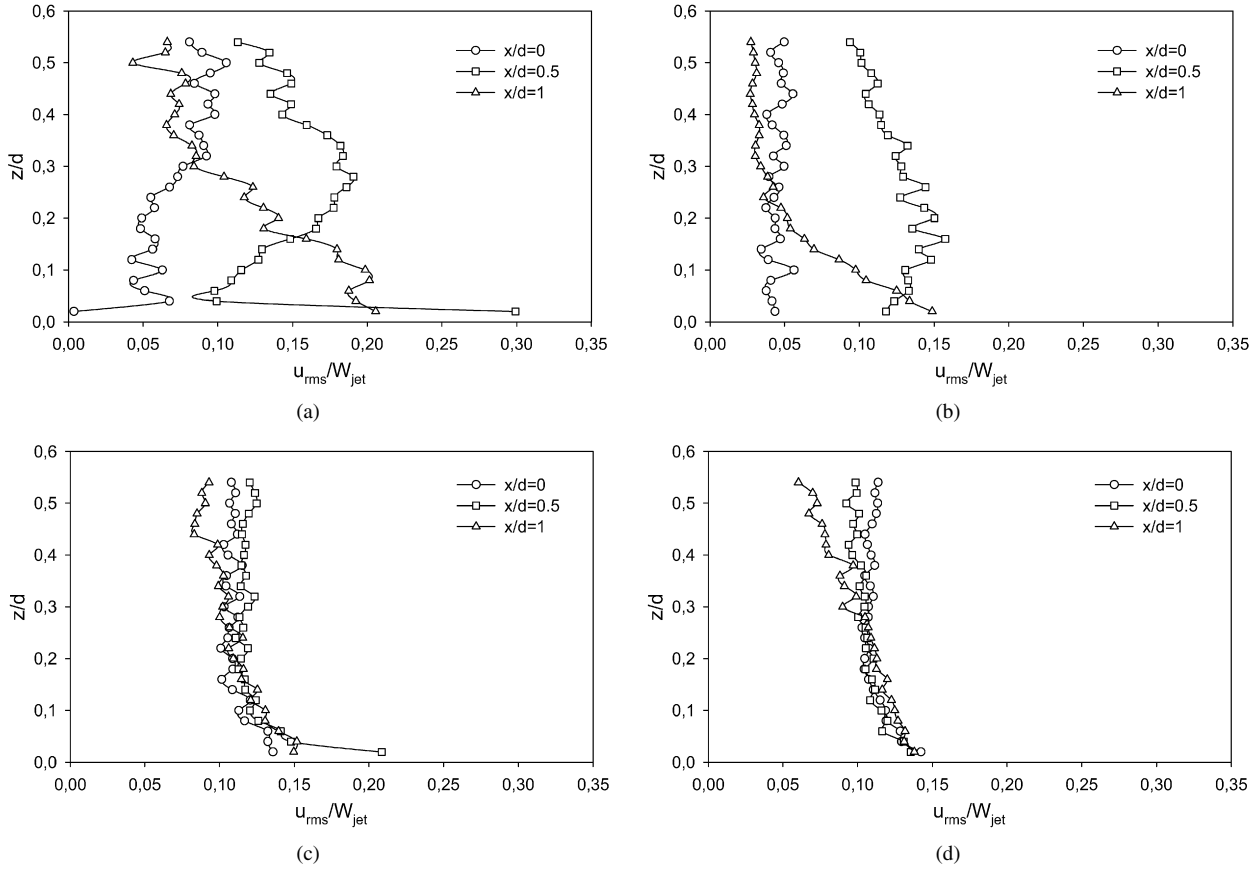

Fig. 8. LDA radial rms velocity distribution at $x/d = 0$–1 for (a) EJ1, $H/d = 2$, (b) major axis EJ4, $H/d = 2$, (c) EJ1, $H/d = 6$, (d) major axis EJ4, $H/d = 6$. (The target plate is located at $z/d = 0$.)

ular distances from the plate. At radial locations greater than $x/d = 1$, deceleration of the flow was observed for all cases. At $H/d = 2$ different boundary layer profiles were obtained for circular and elliptic jets. With increasing jet to plate distance profiles become similar. It is an indication of the effect of jet exit geometry conditions, which decrease with increasing jet to plate distance.

Radial velocity measurements showed the flow acceleration starting from impinging point on. In these measurements, maximum radial velocities were obtained between $x/d = 0.5$ and 1. In order to further investigate this region, turbulence intensities corresponding to radial velocity profiles in the region $x/d = 0$–1 were obtained and presented in Fig. 8 for circular and elliptic jets. Fig. 8 (a, b) shows measurement results for dimensionless jet to target distance 2. At the closest point to the impinging plate largest rms values were obtained at $x/d = 0.5$ and $x/d = 1$ for circular and elliptic jets, respectively. While approaching the plate, turbulence intensities at $x/d = 1$ continuously increase. Measurements at $H/d = 6$ are shown in Fig. 8 (c, d). Especially for the elliptic jet, rms values closer to the impinging point reach an almost constant value irrespective of radial location. At the nearest point to the target plate, maximum turbulence intensities were obtained at $x/d = 0.5$ for the circular jet. Even though the differences are small, the highest turbulence intensity for the elliptic jet was obtained at the center line.

Jet velocity continuously changes starting from the jet exit onward, as a result of the interaction with the surrounding air. To determine the role of jet to plate distance and jet geometry on the jet velocities in the jet center line and close vicinity, axial velocities were measured. Fig. 9 shows the normalized axial velocities at the jet centerline and close vicinity as a function of axial distance from the jet exit. Centerline axial velocities first gradually decrease for circular and elliptic jets, than, as the target plate is approached, the centerline velocity drops rapidly. In addition to the centerline, axial velocities were also measured at some other radial distances. Because of the sharp edged orifices and size of the LDA measurement volume, at points close to the jet exit, very small axial velocities were measured even in the jet especially for circular jets and for the major axis direction of the elliptic jet. Fig. 9 (e, f) shows the axial velocity measurements in the minor axis direction. High spreading rate of the jet along this axis can easily be seen from the increasing velocity values with increasing distance from the jet exit at radial positions $y/d = 0.3$, 0.4, 0.5, which are out of the jet edge.

In addition to jet velocities, turbulence level in the jet also changes. Even, an initially laminar jet at the exit can become turbulent at down stream positions from the jet exit. Near target plate measurements could also be used to analyze heat transfer results. Therefore turbulence intensities corresponding to axial velocities were obtained and presented in Fig. 10. Close to the jet exit, for the circular jet and in the minor axis direc-

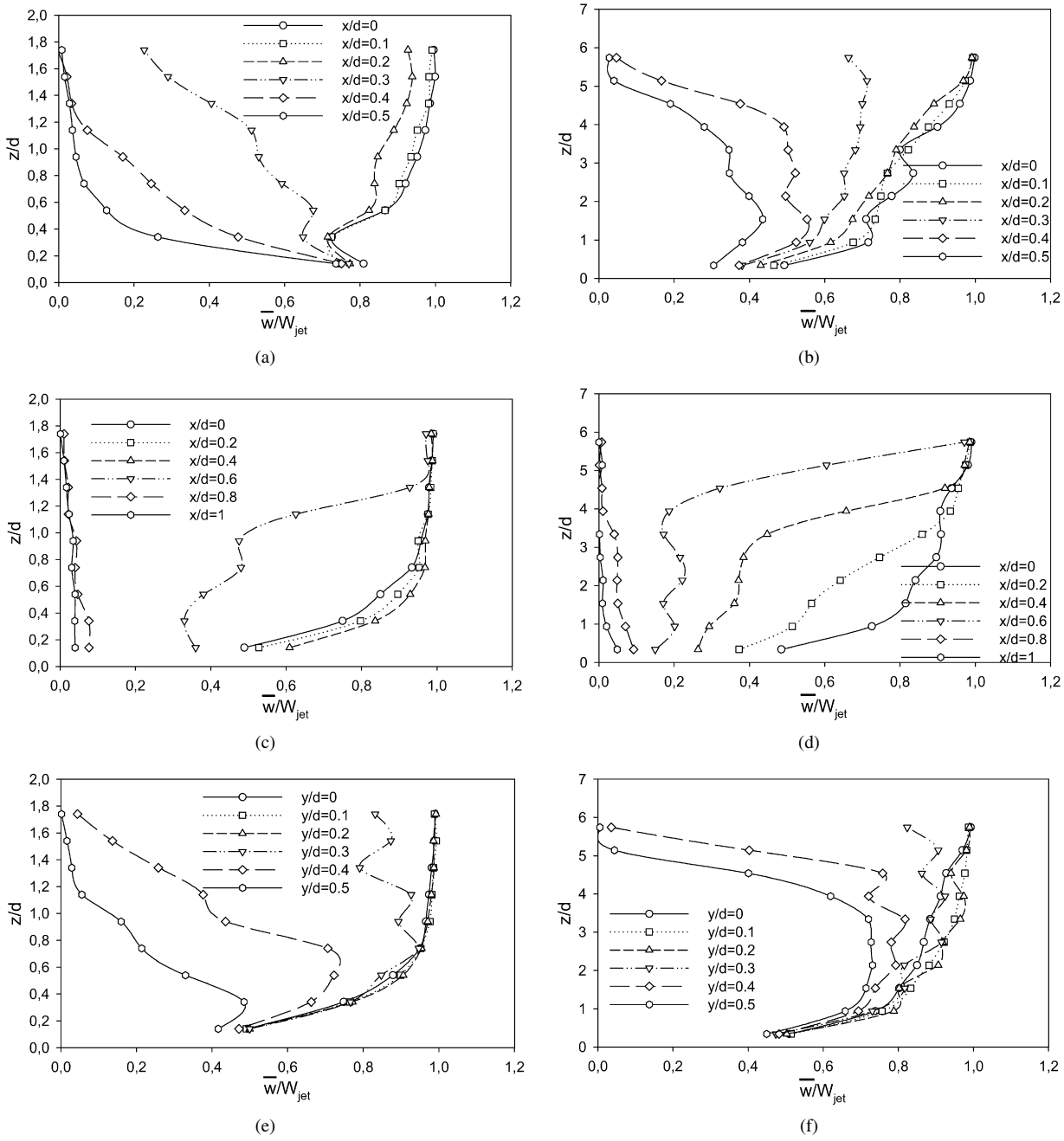

Fig. 9. LDA axial velocity distribution in the close vicinity of the jet centerline for (a) EJ1, $H/d = 2$, (b) EJ1, $H/d = 6$, (c) major axis EJ4, $H/d = 2$ (d) major axis EJ4, $H/d = 6$, (e) minor axis EJ4, $H/d = 2$, (f) minor axis EJ4, $H/d = 6$. (The target plate is located at $z/d = 0$.)

tion of the elliptic jet, maximum rms velocities were obtained at $x/d = 0.3$ and $y/d = 0.3$, respectively. In the major axis, very close rms values were measured at different radial positions close to the jet exit. For minor axis direction of the elliptic jet, position of the maximum rms value continuously changes along the distance from the jet exit onwards. At the closest point to the target plate, maximum rms values along this axis were obtained at $y/d = 0.5$ and 0.3 for $H/d = 2$ and 6, respectively. For $H/d = 2$, at the closest point to the target plate in the long axis direction, the highest rms velocity was obtained at a radial distance of $x/d = 0.6$. The radial position of the maximum rms velocity shifts towards the jet centerline, and was obtained at $x/d = 0.2$ for the dimensionless jet to target plate distance of 6.

By using the instantaneous and mean velocity components, Reynolds shear stress distributions were calculated in the close vicinity of the jet centerline and out of jet edge for the circular jet and major axis direction of the elliptic jet. The results are shown in Figs. 11 and 12. As shown in Fig. 11, Reynolds stresses were almost zero or close to zero along the jet centerline for all cases and non-zero values were obtained in the other high speed locations. Zero Reynolds stresses were also observed in the region outside the jet edge as shown in Fig. 12. In this region, non-zero values were obtained close to the tar-

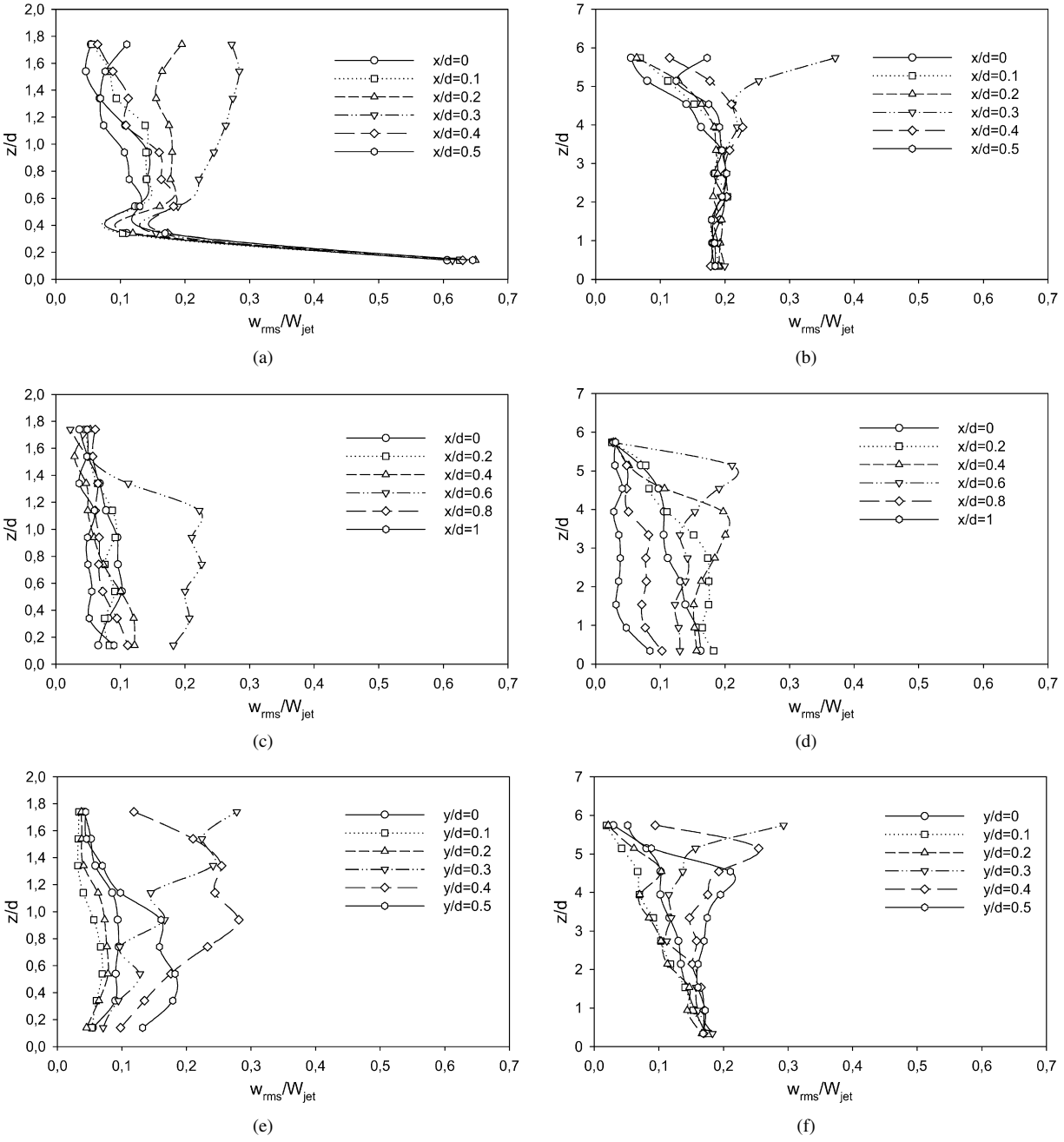

Fig. 10. LDA axial rms velocity distribution in the close vicinity of the jet centerline for (a) EJ1, $H/d = 2$, (b) EJ1, $H/d = 6$, (c) major axis EJ4, $H/d = 2$, (d) major axis EJ4, $H/d = 6$, (e) minor axis EJ4, $H/d = 2$, (f) minor axis EJ4, $H/d = 6$. (The target plate is located at $z/d = 0$.)

get plate. Higher values in the Reynolds stress show that most of the transverse momentum transfer occurs in the high speed region. The negative Reynolds stress is associated with the negative production of turbulence [28]. It always happens in the non-pairing state of a single vortex or in the latter part of the vortex merging, and can be explained by the vortex nutation idea [6].

For the confined circular and elliptic jet geometries of the LDA measurements, local heat transfer characteristics have been obtained numerically by using the Lam–Bramhorst low Reynolds number k–ε, model for dimensionless jet to plate distances 2, 6, 12 at Reynolds number 10 000. Fig. 13 shows the local heat transfer distribution along the major and minor axis directions. In addition to the stagnation point values, inner peaks in the heat transfer rates were observed in major and minor axis directions. In the stagnation region, higher heat transfer rates were obtained in the major axis direction with elliptic jets especially at $H/d = 2$ and 6. Through LDA measurements detailed flow field data were obtained for the outflow region and near target plate region for circular and elliptic jets. The outflow region is of less importance to the heat transfer from the impinging jets. On the other hand, the near target plate region measurements of velocity and turbulence could be used to further elaborate the heat transfer results. From the near target

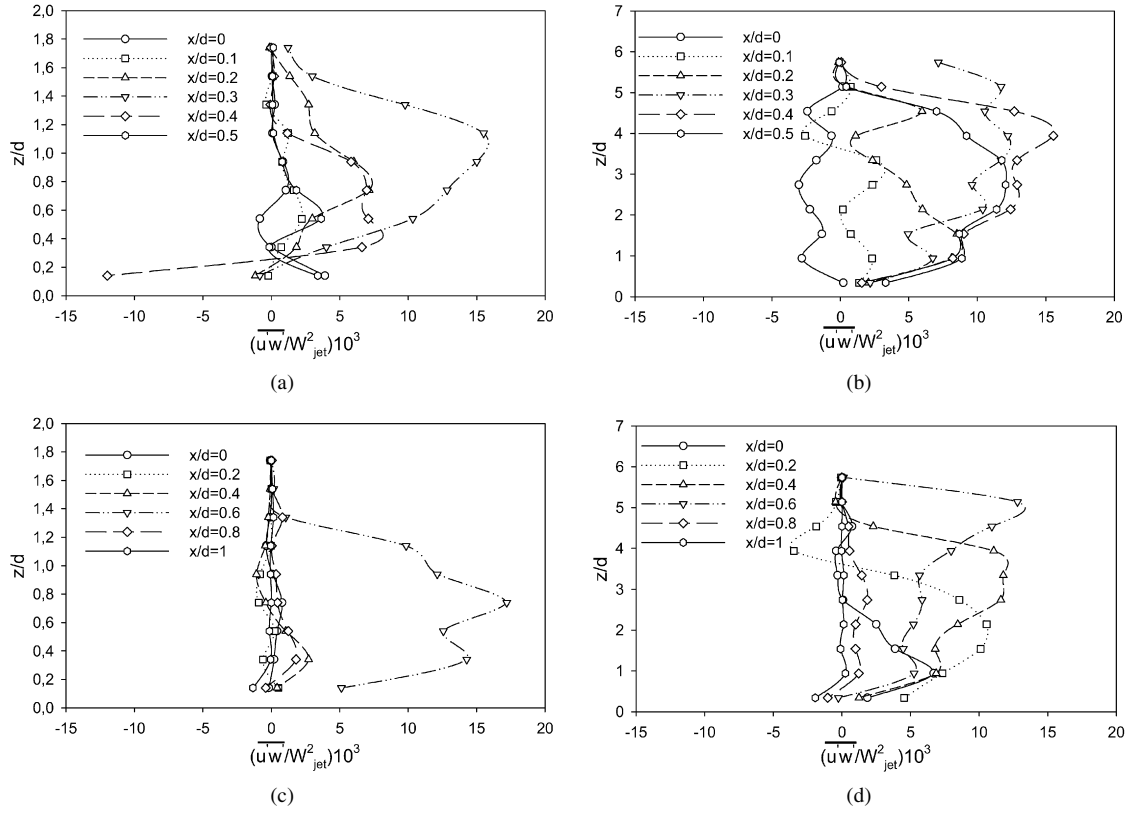

Fig. 11. LDA Reynolds stress distribution in the close vicinity of the jet centerline for (a) EJ1, $H/d = 2$, (b) EJ1, $H/d = 6$, (c) major axis EJ4, $H/d = 2$, (d) major axis EJ4, $H/d = 6$. (The target plate is located at $z/d = 0$.)

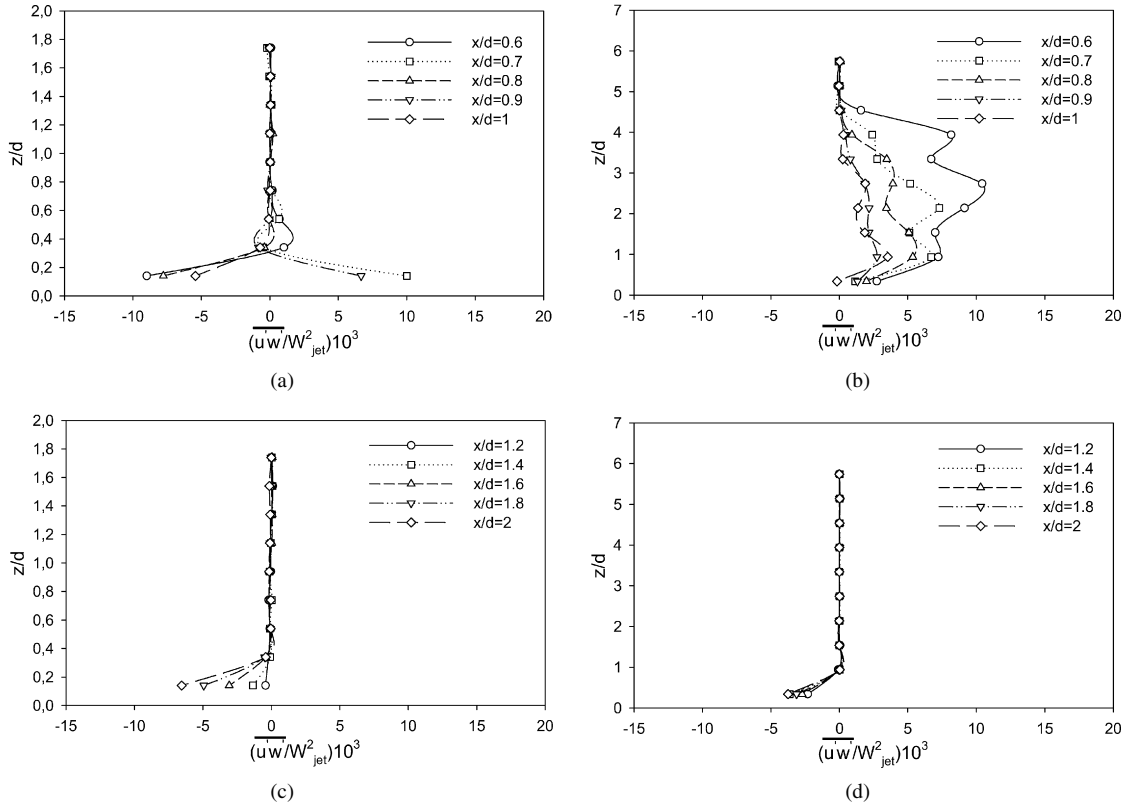

Fig. 12. LDA Reynolds stress distribution outside the jet edge for (a) EJ1, $H/d = 2$, (b) EJ1, $H/d = 6$, (c) major axis EJ4, $H/d = 2$, (d) major axis EJ4, $H/d = 6$. (The target plate is located at $z/d = 0$.)

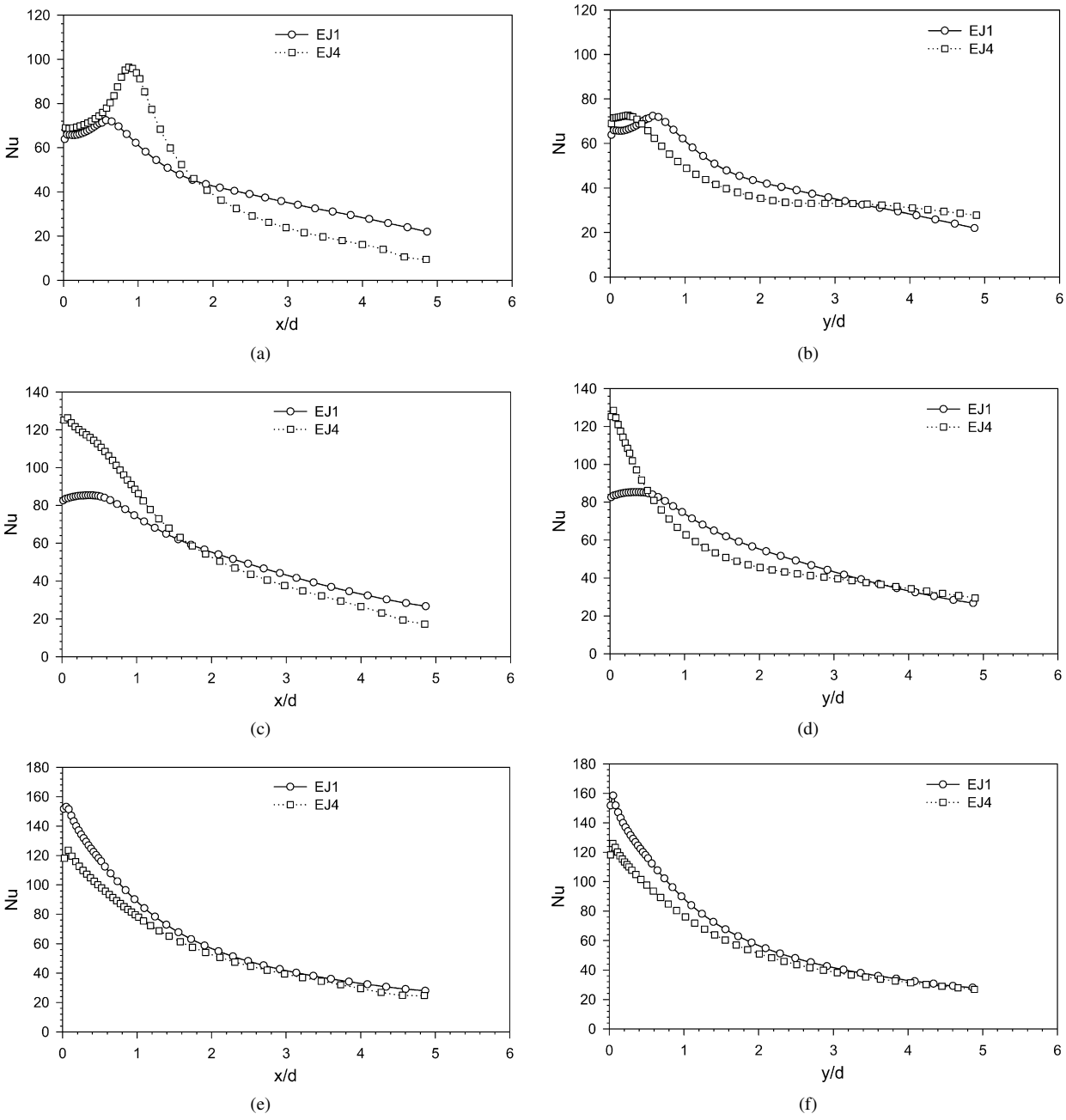

Fig. 13. Effect of jet geometry on local Nusselt number distribution at $Re = 10\,000$ for (a) major axis $H/d = 2$, (b) minor axis $H/d = 2$, (c) major axis $H/d = 6$, (d) minor axis $H/d = 6$, (e) major axis $H/d = 12$, (f) minor axis $H/d = 12$.

plate region LDA measurements, maximum axial rms velocities were obtained in the region 0.6d from the centerline, and maximum radial velocities were obtained between $x/d = 0.5$ and 1. Analysis of flow field measurements and numerical heat transfer results show that inner peaks in local heat transfer could be related to locations of maximum turbulence intensities in the jet and radial flow acceleration along the wall for both circular and elliptic jets. Because of the strong mixing, elliptic jets have shorter potential core lengths. When the dimensionless jet to plate distance is increased to 12, the elliptic jet will have lost most of its momentum. As a result, in the stagnation region, the circular jet gives higher heat transfer rates in the major and minor axis directions compared to the elliptic jet. Numerical results showed that with increasing jet to plate distance the effect of jet geometry on the heat transfer decreased. Similar findings were obtained from the flow field characteristics obtained from LDA measurements, that also became more similar for elliptic and circular jets at the high jet to plate distance.

5. Conclusions

The flow field of confined circular and elliptic jets was investigated through velocity and turbulence measurements using laser Doppler anemometry, for two different jet to plate distances at Reynolds number 10 000. In addition, local heat transfer characteristics were obtained numerically for dimen-

sionless jet to plate distances 2, 6, 12 at Reynolds number 10 000. A toroidal recirculation zone, which is the characteristic of confined jets, has been observed at dimensionless jet to target spacing 2. Much higher spreading rates in the minor axis direction of the elliptic jet have also been mapped. An increase in the jet to plate distance reduced the differences between circular and elliptic jet flow fields. Combined analysis of LDA measurements and numerical results showed that there could be a linkage between local heat transfer rates and turbulence intensities in the jet, and radial flow acceleration along the wall for both circular and elliptic jets. To further analyze about the relationship it is necessary to conduct research with optical measurement and flow visualization techniques for a broader range of parameters including jet to plate distance, jet geometries and jet exit velocities.

Acknowledgements

Financial support of this study by the research fund of the Gazi University under Grant No. BAP 06/2005-51 and State Planning Organization of Turkey under Grant No. DPT-2003K120470-28 is gratefully acknowledged.

References

[1] R. Viskanta, Heat transfer to impinging isothermal gas and flame jets, Experimental Thermal and Fluid Science 6 (1993) 111–134.
[2] K. Jambunathan, E. Lai, M.A. Moss, B.L. Button, A review of heat transfer data for single circular jet impingement, International Journal of Heat and Fluid Flow 13 (1992) 106–115.
[3] R. Gardon, J.C. Akfirat, The role of turbulence in determining the heat transfer characteristics of impinging jets, International Journal of Heat and Mass Transfer 8 (1965) 1261–1272.
[4] R. Gardon, J.C. Akfirat, Heat transfer characteristics of impinging two dimensional air jets, Journal of Heat Transfer 88 (1966) 101–108.
[5] F. Hussain, H.S. Husain, Elliptic jets, Part 1. Characteristics of unexcited and excited jets, Journal of Fluid Mechanics 208 (1989) 257–320.
[6] C.M. Hoo, E. Gutmark, Vortex induction and mass entrainment in a small aspect ratio elliptic jet, Journal of Fluid Mechanics 179 (1987) 383–405.
[7] S.J. Lee, J.H. Lee, D.H. Lee, Local heat transfer measurements from an elliptic jet impinging on a flat plate using liquid crystal, International Journal of Heat and Mass Transfer 37 (1994) 967–976.
[8] J. Lee, S.J. Lee, The effect of nozzle aspect ratio on stagnation region heat transfer characteristics of elliptic impinging jet, International Journal of Heat and Mass Transfer 43 (2000) 555–575.
[9] W.M. Yan, S.C. Mei, H.C. Liu, C.Y. Soong, W.J. Yang, Measurement of detailed heat transfer on a surface under arrays of impinging elliptic jets by a transient liquid crystal technique, International Journal of Heat and Mass Transfer 47 (2004) 5235–5245.
[10] W.M. Yan, H.C. Liu, C.Y. Soong, W.J. Yang, Experimental study of impinging heat transfer along rib-roughened walls by using transient liquid crystal technique, International Journal of Heat and Mass Transfer 48 (2005) 2420–2428.
[11] W.M. Yan, S.C. Mei, Measurement of detailed heat transfer along rib-roughened surface under arrays of impinging elliptic jets, International Journal of Heat and Mass Transfer 49 (2006) 157–170.
[12] T.J. Craft, L.C.W. Graham, B.E. Launder, Impinging jet studies for turbulence model assessment—II. An examination of the performance of four turbulence models, International Journal of Heat and Mass Transfer 36 (1993) 2685–2697.
[13] S.M. Hosseinalipour, A.S. Mujumdar, Comparative evaluation of different turbulence models for confined impinging and opposing jet flows, Numerical Heat Transfer, Part A 28 (1995) 647–666.
[14] S.J. Wang, A.S. Mujumdar, A comparative study of five low Reynolds number k–ε models for impingement heat transfer, Applied Thermal Engineering 25 (2005) 31–44.
[15] Y.L. Shi, M.B. Ray, A.S. Mujumdar, Computational study of impingement heat transfer under a turbulent slot jet, Industrial and Engineering Chemistry Research 41 (2002) 4643–4651.
[16] M. Dianat, M. Fairweather, W.P. Jones, Predictions of the concentration field of an impacting turbulent jets, in: Proc. 10th Turbulent Shear Flows Symposium, The Pennsylvania State University, University Park, 1995.
[17] M.M. Gibson, R.D. Harper, Calculation of impinging jet heat transfer with the low-Reynolds-number q–ζ turbulence model, International Journal of Heat and Fluid Flow 18 (1997) 80–87.
[18] J.A. Fitzgerald, S.V. Garimella, A study of the flow field of a confined and submerged impinging jet, International Journal of Heat and Mass Transfer 41 (1998) 1025–1034.
[19] S.V. Garimella, Heat transfer and flow fields in confined jet impingement, in: Annual Review of Heat Transfer, vol. 11, Begell House, New York, 2000, pp. 413–494 (Chapter 7).
[20] M.F. Koseoglu, Experimental and numerical investigation of electronics equipment cooling with impinging jets, PhD thesis, Gazi University, Ankara, Turkey, 2007.
[21] DANTEC, LDA System's User Manual, 2005.
[22] H.E. Albrecht, M. Borys, N. Damaschke, C. Tropea, Laser Doppler and Phase Doppler Measurement Techniques, Springer-Verlag, Berlin–Heidelberg, 2003.
[23] B.E. Launder, D.B. Spalding, The numerical computation of turbulent flows, Computer Methods in Applied Mechanics and Engineering 3 (1974) 269–289.
[24] S.Z. Shuja, B.S. Yilbas, M.O. Budair, Gas jet impingement on a surface having a limited constant heat flux area: various turbulence models, Numerical Heat Transfer, Part A 36 (1999) 171–200.
[25] S.Z. Shuja, B.S. Yilbas, Pulsative heating of surfaces, International Journal of Heat and Mass Transfer 41 (1998) 3899–3918.
[26] V.C. Patel, R.W. Rodi, G. Scheuere, Turbulence models for near wall and low Reynolds number flows: A review, AIAA Journal 23 (1985) 1308–1319.
[27] D.B. Spalding, The PHOENICS Encyclopedia, London.
[28] D. Oster, I. Wygnanski, The forced mixing layer between parallel streams, Journal of Fluid Mechanics 123 (1982) 91–130.